Corrosion Behavior and Hardness of Binary Mg Alloys Produced via High-Energy Ball-Milling and Subsequent Spark Plasma Sintering

Mohammad Umar Farooq Khan,[‡,,***] Taban Larimian,[***] T. Borkar,[***] and R.K. Gupta[**,***]*

In this work, nine nanocrystalline binary Mg alloys were synthesized by high-energy ball milling. The compositions, Mg-5 wt% M (M-Cr, Ge, Mn, Mo, Ta, Ti, V, Y, and Zn), were milled with the objective of achieving non-equilibrium alloying. The milled alloys were consolidated via cold compaction (CC) at 25°C and spark plasma sintering (SPS) at 300°C. X-ray diffraction (XRD) analysis indicated grain refinement below 100 nm, and the scanning electron microscopy revealed homogeneous microstructures for all compositions. XRD analysis revealed that most of the alloys showed a change in the lattice parameter, which indicates the formation of a solid solution. A significant increase in the hardness compared to unmilled Mg was observed for all of the alloys. The corrosion behavior was improved in all of the binary alloys compared to milled Mg. A significant decrease in the cathodic kinetics was evident due to Ge and Zn additions. The influence of the alloying elements on corrosion behavior has been categorized and discussed based on the electrochemical response of their respective binary Mg alloys.

KEY WORDS: high-energy ball milling, magnesium alloys, nanocrystalline alloys, nonequilibrium alloying, spark plasma sintering

INTRODUCTION

Magnesium (Mg) alloys have attracted significant attention for light-weighting in structural applications due to low density and the capability of imparting high specific strength.[1-3] Having an elastic modulus comparable to human bones[4] and excellent biocompatibility,[5] Mg drives interest in biomedical applications.[1-2,6] Its high theoretical energy density is attractive to applications in the field of electronics.[7-8] However, these applications demand an improved strength and controlled corrosion behavior of Mg to fulfill the needs of near-future challenges for its use in industrial applications.[1] Enhanced understanding of the structure-property relationship for Mg alloys, ability to design desired microstructure, and exploration of new compositions are expected to facilitate the development of new Mg alloys with properties closer to other structural alloys used in various engineering applications. Over the years, the study of Mg has brought up the anomalous degradation behavior of Mg in an aqueous environment.[1]

Well-known characteristics for Mg include its extremely low exchange current density for the hydrogen evolution reaction[9] and standard electrode potential being much below the hydrogen stability region,[2] at least at all pH below 14, in the Mg Pourbaix diagram.[2,10] A low exchange current density makes it a poor cathode[9] and due to substantially low electrode potential, the occurrence of the hydrogen evolution is possible even at the anodic overpotentials.[1-2,11] Consequently, many elements, either present as an impurity or for alloying to improve mechanical properties, are known to enhance cathodic reactions and cathodic activation of the corroded surface, which electrochemically balances with a high anodic reaction rate, e.g., the dissolution rate of Mg.[2,11-14] The anodic kinetics get enhanced because of the cathodic activation of the corroded Mg surface, and this is termed as a negative difference effect (NDE).[15-17]

Several alloys have evolved over decades, which exhibit improved mechanical strength but mostly at the expense of corrosion resistance.[1-2] The mechanical strength is enhanced mainly by introducing precipitates or secondary phases, which act as electrochemical heterogeneities and cause corrosion. The strategies to circumvent the issue can be developed by considering processing techniques, alloying elements, or a combination of the two. First, some processing techniques help minimize the uneven composition and size distribution of precipitates or secondary phases to have a lower galvanic corrosion effect. These techniques include continuous stirring of molten liquid followed by cooling,[18] semi-solid stirring,[19] high-pressure die casting,[20] foil metallurgy processing,[21] powder metallurgy followed by hot consolidation,[22] and friction stir welding.[23] Second, besides using techniques to improve corrosion resistance, some elements are shown to directly contribute to the minimization of corrosion current density of Mg, such as Al[24] and Mn,[25] when present in solid solution without noble precipitate formation.[2,26] In contrast, other elements help in uniform distribution of intermetallics such as Zn, Ti, Y, etc., thus rendering them less harmful to the Mg matrix.[2] For

Submitted for publication: July 1, 2020. Revised and accepted: November 17, 2020. Preprint available online: November 17, 2020, https://doi.org/10.5006/3633.
‡ Corresponding authors. E-mail: mk189@zips.uakron.edu.
* Department of Chemical, Biomolecular, and Corrosion Engineering, The University of Akron, Akron, Ohio, 44325.
** Department Materials Science and Engineering, North Carolina State University, Raleigh, North Carolina, 27606.
*** Department of Mechanical Engineering, Washkevicz College of Engineering, Cleveland State University, Cleveland, Ohio, 44115.

ISSN 0010-9312 (print), 1938-159X (online)

instance, Zn is added to Mg-Al and Mg-Zr-rare earth (RE) alloys, and Y is added to commercial AZ series Mg alloys.[2] A unique category of elements known as cathodic poisons, e.g., Ge, Sn, As, etc., does not increase the cathodic kinetics; instead, they lower the NDE effect.[27] Specific element addition can also help in the refinement of grains, such as Zn, Al, and Zr[2] but not necessarily in lowering the corrosion kinetics. Some other elements, such as Cr, Mo, Ta, V, and Nb, akin to their role shown in literature for positively modifying the dissolution characteristics of Al using high-energy ball-milling (HEBM),[28-30] can potentially be helpful in improving corrosion resistance for Mg.

Decreasing the negative influence of the second phase by modifying their compositions or size has been suggested for improving the corrosion behavior of Al alloys.[31-37] Similar concepts can be applied to enhance the corrosion behavior of Mg. Different nonequilibrium Mg and Al alloys, facilitating extended solid solubility of nonconventional alloying elements, have been produced via techniques such as sputter deposition[38-44] and ion implantation.[45-55] A few examples of sputter-deposited alloys include Mg-Y,[38] Al-Mo,[40-41] Al-Ta,[42] Al-Ti,[43] and Al-Ge.[44] Ion implantation examples for Mg alloys include Y on AZ31,[45] Ti on AZ91,[46] Zn on Mg-Ca,[50] Ta on AZ31,[51] Mg-Ti,[53] and Mg-Y and Mg-Gd.[54] Examples for ion implantation in Al alloys are Al-Mo,[55] Al-Cr and Al-Cr-Mo,[47] and N-Si-Ti-Cr in Al 2014 and Al 1100 alloys.[48] The nonconventional alloying elements from the mentioned examples could be listed as Mo, Ti, Ta, Y, Ge, and Cr. Although the two mentioned techniques show a good indication of high solid solubility and refined grains in a finite thickness from the surface, they are not feasible for making bulk parts necessary to be used for industrial applications. Hence, looking for other techniques to achieve the objective of making nonconventional alloys feasible for bulk material is obvious.

The refined grain size and fine distribution of precipitates can also be achieved by utilizing widely used severe plastic deformation techniques such as equal channel angular pressing (ECAP) and HEBM. ECAP has been used to decrease the dissolution due to corrosion by refining grain size of Mg[56-59] and Al[19,60-63] alloys, but it does not help in increasing the solid solubility of alloying elements. On the other hand, HEBM has been utilized to not only refine the grain size and the distribution of precipitates but also could be helpful in forming a supersaturated solid solution of nonconventional elements, as reported for Fe and Al alloys.[29-30] Milling techniques have been previously used for some metal additions into Mg. Mechanical alloying of Mg-Ti systems have shown extended solubility up to 12.5 at% by Liang and Schulz[64] and up to 2.35 at% by Zhou, et al.,[65] on the addition of 20 at% Ti and 0.15 molar fraction Ti during milling, respectively. Extended solubility was also reported for a few other elements including Y and Zn by Liang and Schulz.[66] Solid solution formation for Mn in Mg using ball milling was suggested by Salleh, et al.[67] On the other hand, there are studies reporting negligible alloying after 20 h of milling on the addition of certain metals including Cr, Mo, V, and Y.[68] Addition of Ge into Mg has been previously attempted using ball milling by Clark, et al. (33% addition), which resulted in the intermetallic formation and unmilled Ge.[69] Hence, there is merit in further exploring the application of HEBM in producing Mg alloys containing nonconventional alloying elements and studying the corrosion performance of the ball-milled Mg alloys.

The work herein investigates the use of HEBM and subsequent spark plasma sintering in producing Mg alloys containing 5 wt% of nonconventional alloying elements (M: Ge, Mn, Mo, Cr, Ta, Ti, V, Y, and Zn). The produced nanocrystalline binary Mg alloys, with some exhibiting better strength than commercial alloys, were categorized based on their elements' respective influence in the electrochemical polarization curve of Mg. Such categorization is expected to facilitate the development of Mg alloys with high strength and the selection of alloying elements in modifying corrosion resistance of commercial Mg alloys.

EXPERIMENTAL PROCEDURES

2.1 | Materials and Mechanical Milling

The powders involved in mechanical alloying are Mg, Cr, Ge, Mn, Mo, Ta, Ti, V, Y, and Zn; the supplier and composition of the as-received powders are given in Table S1 (Supplemental Material). The powders in the weight ratio Mg/M:19/1 (M- Ge, Mn, Mo, Cr, Ta, Ti, V, Y, and Zn) were placed in the milling jars in an inert gas (high purity Ar atmosphere, O_2 < 25 ppm). Stearic acid (1.5 wt%) was added as a process controlling agent to avoid agglomeration of powders. The metal powders and stearic acid were loaded in a tungsten carbide (WC) jar along with the WC balls (10 mm diameter) followed by the encasing of jars into ball mill fixtures. The milling jar contained a total weight of 10 g powder, maintaining a ball-to-powder weight ratio of 40:1. Powder-loaded jars were then set on to the planetary ball mill that operated at 280 rpm. After every 1 h of milling, the mill was paused for 30 min to allow cooling of the jars and avoid excess heat. After milling, the jar was opened inside the glove box for collecting the resulting material. The produced alloys are termed as Mg-5M where M is either Ge, Mn, Mo, Cr, Ta, Ti, V, Y, or Zn. Alloying content was kept constant (5 wt%) for each alloy.

2.2 | Powder Compaction/Consolidation

Cold compaction (CC): Milled alloy powders were compacted at room temperature (25°C) using a uniaxial hydraulic press load of 3 GPa for 10 min on a WC die where powder material was supported by WC punches. The resulting cylindrical pellet had a diameter of 7 mm and a thickness of 1.5 mm to 2 mm.

Spark plasma sintering (SPS): The milled Mg-5M alloys were consolidated under uniaxial pressure of 200 MPa at 300°C in a WC die of 10 mm diameter using SPS machine (Thermal Technology[†] 10-3). To maintain the conductivity and to avoid any sticking, a graphite sheet was placed between the powder-WC die interface, and the powder WC punches.

2.3 | Characterization Using X-Ray Diffraction and Scanning Electron Microscopy

As-milled alloy powders and alloy samples consolidated by SPS were studied using Rigaku[†] x-ray diffractometer (XRD) for analyzing the phases present in them. A Cu-K_α radiation source (λ = 0.1541 nm) with a tube voltage of 40 kV and a tube current of 44 mA was used for XRD studies. These alloys were scanned between the 2θ range of 25° to 85° with a scan rate of 1°/min and a step size of 0.01°. For repeatability of milling, XRD was performed for different Mg milling experiments (grain size is reported in Figure S1 of the Supplemental Material). The consolidated samples were ground to 1200 grit SiC sandpaper for XRD analysis and then polished up to 0.05 μm surface finish using diamond suspensions followed by colloidal silica + alumina suspension for scanning electron microscropy (SEM)/energy-dispersive x-ray spectroscopy (EDS) studies. After grinding, the samples were ultrasonically cleaned for 5 min with ethanol and also after each subsequent polishing step.

[†] Trade name.

The SPS alloy samples were analyzed using XRD for phase and grain size determination. The diffractometer configuration and scanning parameters used were the same as mentioned above for all Mg-5M alloys SPS at 300°C under 200 MPa pressure for 5 min. The grain size was calculated using Scherer's equation[70] and averaged for three highest-intensity Mg peaks, after removing the instrumental broadening, which was determined using annealed pure Mg powder.

The microstructural study of SPS alloys was performed using a Tescan Lyra 3† focused ion beam field-emission SEM (FIB-FESEM) system in backscattered electron (BSE) mode with an accelerating voltage of 20 kV while maintaining a working distance of 9 mm to 10 mm. EDS was also performed in the same instrument to analyze the composition of different phases present in the microstructure. The quantification of bright phases was determined using ImageJ† software for SPS alloys.

2.4 | Density

The experimental density of samples consolidated by CC and SPS were determined using Sartorius Quintix65-1S† equipped with the attached YDK03† density kit. Before measuring the density, all of the samples were ground up to 1200 grit size SiC paper, and the temperature of the ethanol was measured and accounted for every density measurement. The measurement involved weighing in air and weighing while immersed in ethanol. After weighing in ethanol, the sample was dried with an air blower before going for the next measurement. For each sample, the measurements were repeated at least five times.

2.5 | Hardness

The alloys consolidated using SPS were ground up to 1200 grit size SiC before hardness measurements, whereas CC samples were used as consolidated having a smooth surface impression from the WC punches ground to 1200 grit SiC sandpaper. Hardness was measured using a Vickers microindenter (Beuhler-Wilson Tukon 1202†) by applying 50 gf load with a dwell time of 10 s, where 10 measurements were taken for each sample while maintaining the distance between any two indents >5 times of the indent size.

2.6 | Potentiodynamic Polarization

The corrosion behavior of Mg-5M (M-Ge, Cr, Mn, Mo, Ta, Ti, V, and Zn) alloys consolidated using CC and SPS were investigated by potentiodynamic polarization (PDP) test using a Biologic VMP-300† potentiostat. The surface of the samples was ground up to 1200 grit size SiC sandpaper for all PDP tests. A conventional three-electrode setup was used in a flat cell from Princeton Applied Research†, having platinum mesh as a counter electrode where standard calomel electrode (SCE) was used as a reference. All PDP tests were performed in 0.1 M NaCl solution exposed to air at room temperature (25°C). The open-circuit potential (OCP) of the samples was monitored for 20 min before commencing the PDP tests. Potential scans started from 250 mV below the OCP, upward with a scan rate of 1 mV/s until an anodic current of 10 mA/cm^2 was reached. PDP tests were performed at least three times.

RESULTS

3.1 | X-Ray Diffraction Analysis

The x-ray diffraction (XRD) scans for the ball-milled Mg-5M (M-Cr, Ge, Mn, Mo, Ta, Ti, V, Y, and Zn) alloys are shown in Figure 1(a). Mg-5Zn alloy showed peaks corresponding to only Mg. All other alloys showed additional peaks corresponding to either alloying elements, intermetallic compounds, or oxides. The alloys having no intermetallic compound or oxide formation (Cr, Mn, Mo, and Al) are shown in Figure 1(a), whereas alloys which formed intermetallic compound and oxides are plotted in Figures 1(b) and (c), respectively. Figure 1(d) shows the zoomed-in comparison of the highest intensity Mg peak with (110) orientation for all of the alloying additions in as-milled conditions. The elemental peak for Cr, Mn, and Mo was observed (Figure 1[a]). Alloys containing Ta, Ti, and V showed the peaks corresponding to their oxides as well (Figure 1[b]). The oxide formation may be attributed to the possible gettering effect similar to that observed or utilized in previous studies on Ti,[71-73] Ta,[74-78] and V,[77-79] which has been reported to act as a getter of oxygen in many processes, including powder metallurgy.[72,76] Mg-5Ge and Mg-5Y showed the presence of intermetallic such as Mg_2Ge and Mg_aY_b ($Mg_2Y/Mg_{24}Y_5$), respectively. Relatively higher intensities were observed for elemental peaks of Mo and Ta (Figures 1[a] and [c], respectively). whereas the intensity of elemental peaks was low for Mn and V (Figures 1[a] and [c], respectively).

Figures 2(a) through (c) show the XRD plots for SPS Mg-5M alloys where Mg-5Cr, Mg-5Mo, and Mg-5Mn did not form any intermetallic or oxide (Figure 2[a]); Mg-5Ge and Mg-5Y predominantly showed intermetallic formation with small peak for GeO_2 for Mg5Ge (Figure 2[b]); and Mg-5Ta, Mg-5Ti, and Mg-5V showed peaks corresponding to the oxides (Figure 2[c]). Mg-5Zn showed both intermetallic and oxide formation (Figure 2[c]). The elemental peak was observed for Cr, Mn, Mo, Ta, Zn, and Y (Figures 2[a] through [c]). Figure 2(d) shows the zoomed-in comparison of the highest intensity Mg peak with (110) orientation for all of the alloying additions after SPS. From Figures 1(a) through (c) and 2(a) through (c), it can be observed that there were no oxides of Mg in the milled powder condition, whereas after SPS MgO peak was observed suggesting oxidation of Mg during the SPS process. Moreover, small intensity peaks of MgC_2 and graphite/MgWO were observed for all SPS processed samples and could be attributed due to pick up from graphite foil wrapped for SPS or W from milling, which clustered during SPS. A mixed oxide peak was observed for SPS Mg-5Zn as MgZnO (Figure 2[c]). The intensity ratio for various phases including elemental phase, intermetallic phase, MgO, and oxide phase of the added element with respect to Mg intensity was determined and listed in the Supplemental Material (Table S2). Mo has the highest fraction of elemental portion in the microstructure followed by Ta, while others have a smaller fraction of the unalloyed elements. The highest MgO fraction was obtained for Mg-5Zn followed by Mg-5Y and Mg-5Mo (Table S2).

The zoomed-in scans of the alloys in Figures 1(d) and 2(d) show a shift in the highest intensity Mg peak (011). The peak shift was toward lower 2θ values for all of the milled alloys except in the case of Zn addition, for which the Mg peak showed a significant shift toward higher 2θ values. The change in the 2θ values can be understood by considering the theoretical atomic diameter of the elements, which suggests that these elements have a larger atomic size than Mg except in the case of Ge.[80] Hence, most of them increased the lattice parameter of Mg after HEBM. Out of these elements Ti, V, Mo, Ta, and Ge have negligible solid solubility, and hence, having peak shifts in these cases is remarkable. The peak shift for Zn addition to higher 2θ values has been previously shown.[81] The peak shifts were also noticeable after SPS for all of the alloys, although with higher peak intensities and decreased broadening.

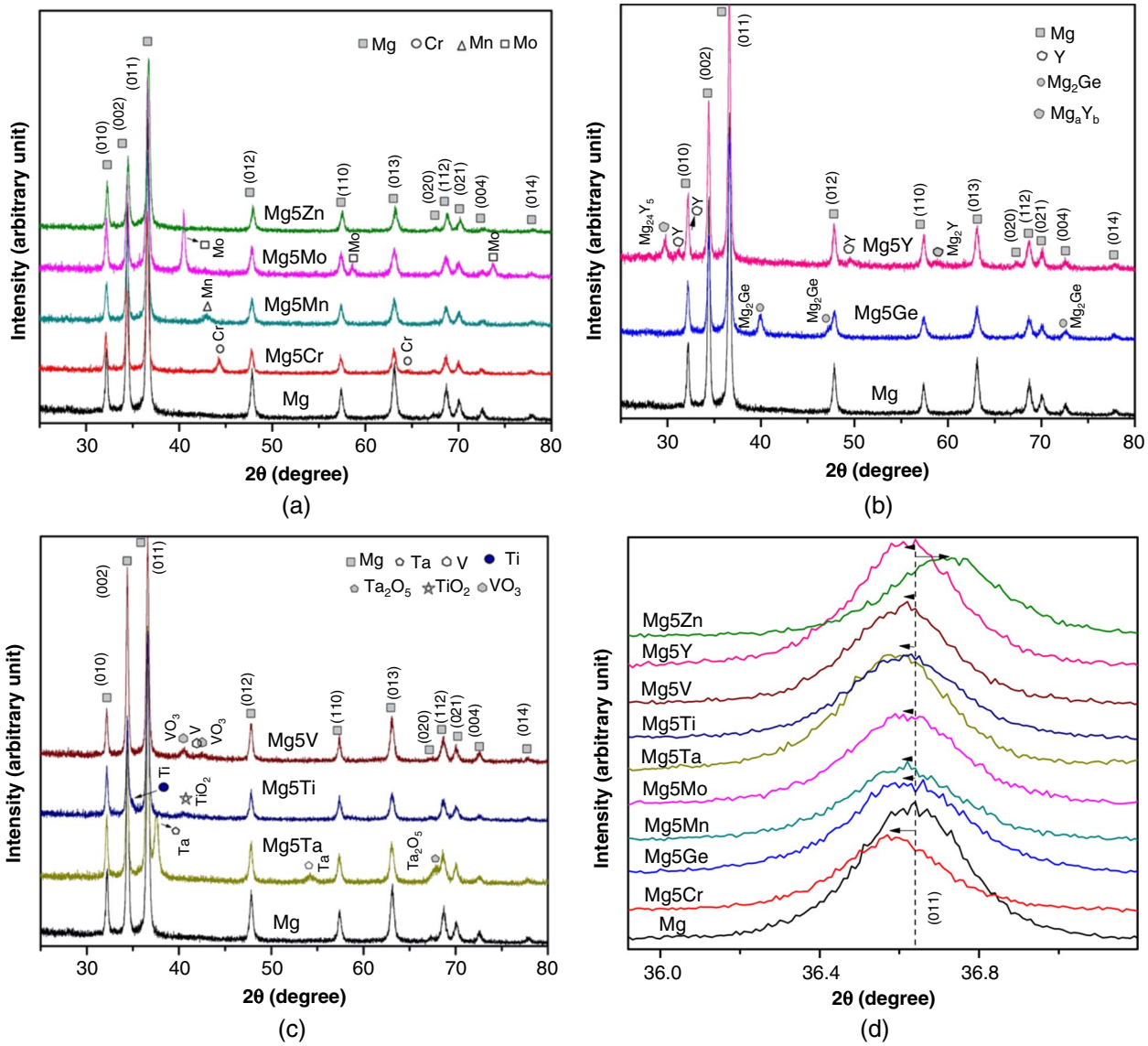

FIGURE 1. *XRD scans for milled Mg-5M powder having (a) Mg and other elemental peaks only (for Cr, Mn, Mo, and Zn addition), (b) Mg and intermetallic peak (for Ge and Y addition), (c) Mg and oxide peaks (for Ta, Ti, and V addition), and (d) zoomed-in highest intensity Mg (110) peak compared for all additions.*

The grain size for Mg-5M alloys for milled and SPS conditions have been presented in Figure 3. The grain size, measured through the Scherer's equation,[70] was less than 100 nm for all as-milled Mg and Mg-5M alloys. The grain size, after SPS, expectedly increased for all of the alloys due to the spark plasma sintering temperature. However, for some of the alloys (Mg-5Ge, Mg-5Mn, and Mg-5Mo) the grain size remained below 100 nm. In the case of Mg-5Zn, the grain growth after SPS was much higher as compared to other alloys because of the low eutectic and solidus temperatures (<400°C) for the alloy.[82]

3.2 | Microstructural Characterization Using Scanning Electron Microscopy and Energy Dispersive X-Ray Spectroscopy

BSE images for the CC and SPS alloys are shown in Figures 4 and 5, respectively. Pores were observed in the majority of the CC Mg-5M alloys and Mg (Figure 4). SPS reduced the size and number of pores (Figure 5). Interparticle boundaries were observed in Mg, Mg-5Ge, and Mg-5Zn alloys, while SEM images of the alloys did not show interparticle boundaries. A peculiar feature found in the case of Mg-5Ge, Mg-5Zn, and Mg was that the interparticle boundaries were easily noticeable, with the boundaries being darker (Figures 4[b], [i], and [j]). Interparticle boundaries appearing darker indicated with marked arrows were observed for SPS Mg-5Zn (Figure 5). It showed that the atomic number of the alloying elements was higher than that of Mg, and therefore, the unalloyed portion of added elements or intermetallics appeared brighter in the BSE images. This understanding suggests that a lower content of alloying elements was present at the interparticle boundaries of Mg-5Ge and Mg-5Zn (Figures 4[b] and [i], respectively). The oxidized region of Mg appeared darker in the SPS condition (Figure 5[j]). The darker interparticle boundaries diminished on SPS for Mg-5Ge (Figure 5[b]). Whereas in the case of Mg-5Zn (Figures 5[i]), the particle boundaries were contrastingly darker compared to

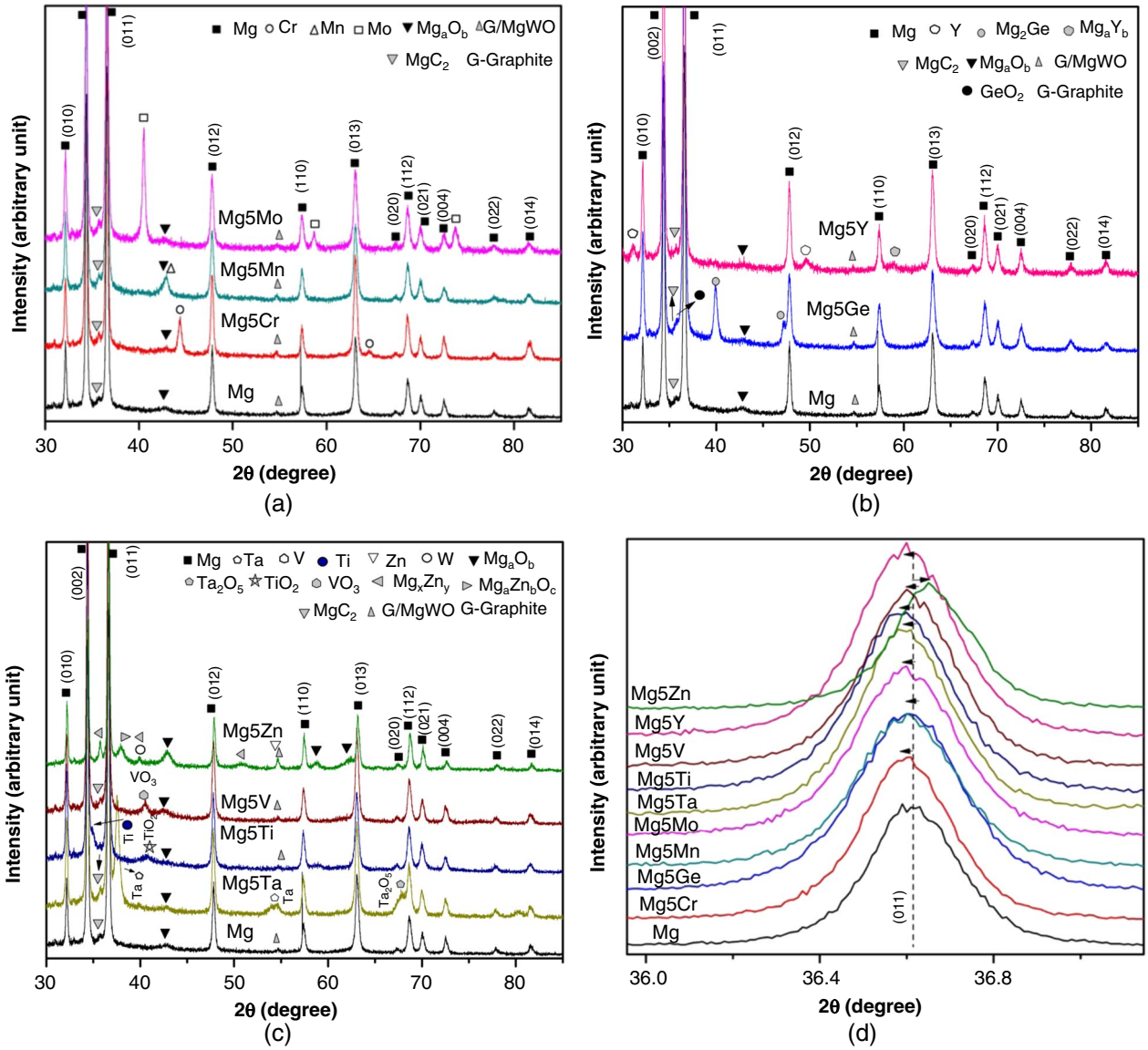

FIGURE 2. *XRD scans for spark plasma sintered Mg-5M alloys having (a) Mg and other elemental peaks only (for Cr, Mn, and Mo addition), (b) Mg and intermetallic peaks (for Ge and Y addition), (c) Mg and oxide peaks (for Ta, Ti, V, and Zn), and (d) zoomed-in region of highest intensity Mg (110) peak compared for all additions.*

that in the CC sample. It can be reasoned that the particle boundaries might be composed of MgO and MgZnO, as observed in XRD results (Figure 2[b]). The oxidized region formed in some alloys (Mg-5Cr, Mg-5Mo, Mg-5Ta, Mg-5Y, and Mg-5Zn) in SPS condition is shown in the Supplemental Material (Figure S2), where the distribution of added elements can also be seen.

In the case of Mg-5Mn, the bright particles seem to be present in varying sizes for the SPS sample, as seen in Figure 5(c), whereas smaller bright particles with pores in adjacent areas were observed in the CC sample (Figure 4[c]). It could be inferred that the bigger bright particles came off during surface preparation in the case of the CC sample, whereas for the SPS Mg-5Mn sample, the bigger bright particles remained intact. These features could be ascribed to better consolidation and bonding during SPS. Similar behavior could be observed for Mg-5Ta alloy, but the particle size was smaller compared to bright particles in Mg-5Mn.

The microstructure of the Mg-5Cr alloy (both CC and SPS) was significantly different than other alloys (Figures 4 and 5), where the bright particles, rich in Cr, were relatively coarser. Mg-5Ge, Mg-5Ti, Mg-5Mo, Mg-5V, Mg-5Ta, and Mg-5Zn showed a uniform distribution of added alloying elements. The fraction of bright particle region on the polished surface was measured using ImageJ† software and the area percentage is listed in Table S3 (Supplemental Material). The highest area fraction of bright particles was observed for Mg-5Y followed by Mg-5Ta.

Pores were observed for all CC Mg-5M alloys except for Mg-5Mo (Figure 4[d]) and Mg-5Y (Figure 4[h]). The pores are indicated with arrows in BSE images of CC samples (Figures 4[a] through [c], [e] through [i]). Qualitatively, a relatively higher number of pores were observed for Mg-5Mn, Mg-5V, Mg-5Zn, and Mg (Figures 4[c], [g], [i], and [j]). Smaller pores were noticed for Mg in CC condition (Figure 4[i]). Exact quantification of pores is avoided because of the presence of oxides and Mg lean regions appearing darker in some cases such as Mg-5V

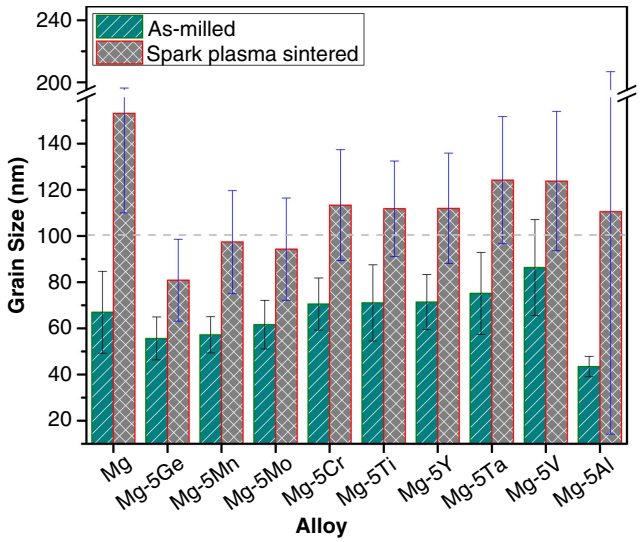

FIGURE 3. *Grain size measured using Scherrer's equation for as-milled and spark plasma sintered Mg-5M (M- Cr, Mn, Ti, Mo, Ge, Ta, V, Y, and Zn) alloys.*

(Figure 4[g]). On the other hand, the pores were significantly suppressed by SPS.

3.3 | Density

Figure 6 shows the comparison of the experimentally measured density with that calculated using the rule of mixture (ROM) for SPS Mg-5M alloys. Experimental density for all of the alloys was significantly lower than that calculated using the ROM. This suggests the presence of porosity in the SPS alloys. The difference in the ROM density and measured density was much higher for Mg-5Ta and Mg-5Mo as compared to other binary alloy compositions (Figure 6).

3.4 | Hardness

A comparative bar chart for the hardness data of ball-milled Mg-5M alloys in CC and SPS consolidation state has been shown in Figure 7. High-temperature exposure during processing such as SPS is expected to decrease the hardness. However, the average Vickers' hardness of all of the binary alloys either remained similar (as in the case of Mg-5Ti and Mg-5Ge) or improved with SPS as compared to CC samples. The fact that the grain size of the alloys increased due to SPS (Figure 3) and the hardness did not decrease that suggests some additional strengthening factor, such as solid solution strengthening and precipitation strengthening, apart from the strengthening due to grain refinement (following Hall-Petch relation). Moreover, it is interesting to observe that the hardness for Mg-5Cr and Mg-5V was lower than that of the milled Mg (Figure 7). These lower hardness values could be correlated to the lesser grain refinement (Figure 3) and insoluble clusters present in their microstructure after HEBM. The highest hardness was obtained for Mg-5Zn alloy in both CC and SPS conditions (Figure 7).

3.5 | Potentiodynamic Polarization

As the microstructural study for the Mg-5M alloys indicated improvement in the consolidation in terms of porosity, the corrosion studies would be most representative for SPS samples. Hence, corrosion data for only SPS samples are being presented here. The OCP of the Mg and Mg-5M alloys in SPS condition is included in the Supplemental Material (Figure S3). Figure 8 shows the potentiodynamic polarization curves for SPS Mg-5M alloy samples tested in 0.1 M NaCl. The lowest cathodic kinetics were observed for Mg-5Ge and then for Mg-5Zn, whereas all other alloys showed higher cathodic kinetics than SPS Mg. Specifically, the highest cathodic kinetics were observed in the case of Mg-5Mo after SPS. The highest anodic kinetics were observed for Mg-5Ge. The lowest anodic kinetics were observed for Mg-5Zn from its corrosion potential (E_{corr}) up to −1,260 mV_{SCE} in comparison to other alloys (Figure 8), after which at higher anodic potentials Mg-5Mo showed the lowest anodic kinetics. Such behavior is seen because the anodic Tafel slope for Mg-5Mo increases faster than that for Mg-5Zn on increasing the potential in the anodic region.

The electrochemical parameters (E_{corr}) and corrosion current density (i_{corr}) have been shown in Figure 9. All of the alloys showed higher E_{corr} compared to Mg except Mg-5Ge, which showed E_{corr} similar to that of as-received SPS Mg. The most noble E_{corr} is evident for Mg-5Mo (Figure 9). Furthermore, the i_{corr} trend was different, exhibiting the lowest i_{corr} value for Mg-5Zn followed by that for Mg-5Ge, both under 100 μA/cm^2. This suggests that the cathodic reaction was severely depressed by the addition of these two elements. As expected, i_{corr} for the milled Mg was the largest. Surprisingly enough, Mg-5Zn had a high E_{corr} next to Mg-5Mo, along with exhibiting the lowest i_{corr}.

DISCUSSION

4.1 | Corrosion Behavior

Most of the spark plasma sintered Mg-5M alloys presented herein showed a noticeable change in both anodic and cathodic current densities, as seen in Figure 8. An increase in the cathodic kinetics with concomitant ennoblement of corrosion potential for all of the alloys, except for Mg-5Ge and Mg-5Zn, was clearly visible (Figure 8). Another reason for a positive shift in the corrosion potential could be ennoblement owing to some alloying during HEBM. Alloying is indicated from the XRD peak (011) shift of the Mg by alloying with Zn, Y, V, Mo, Ti, and Ta (Figures 1[d] and 2[d]). Also, a minor shift is evident for Mn, Ge, and Cr additions. Such shifts are small, but the majority of Mg alloys (reported recently including many commercial alloys[10]) have not shown such a change in corrosion potential along with lower anodic kinetics. Most of the alloys reported by Cain, et al., have E_{corr} values under −1.4 V_{SCE},[10] whereas the E_{corr} values for few alloys here such as Mg-5Zn, Mg-5Mo, and Mg-5V are above −1.4 V_{SCE}. The ennoblement in the case of Mg-Zn is because of the significant alloying, as seen in previous studies.[83] However, for the Mg-5Mo and Mg-5V, the increase in the potential is due to increased cathodic kinetics.

The overall i_{corr} for the SPS alloys was lower than that of SPS Mg. Contrastingly, the review by Esmaily, et al.,[1] suggested an overall increase of the i_{corr} because the increment in the cathodic kinetics overpowered the decrease in anodic kinetics for comparison of Mg alloys, with Mn and Zn being the common alloying additions.[1] The cathodic kinetics for Mg-5Y was similar to that of pure milled Mg. The cathodic kinetics for other alloys shifted right in the following sequence- Mg-5Mn < Mg-5Ta < Mg-5Cr < Mg-5Ti < Mg-5V < Mg-5Mo. Table 1 lists the key comparison between the study of relevant alloys of individual alloying elements with Mg and the kinetics

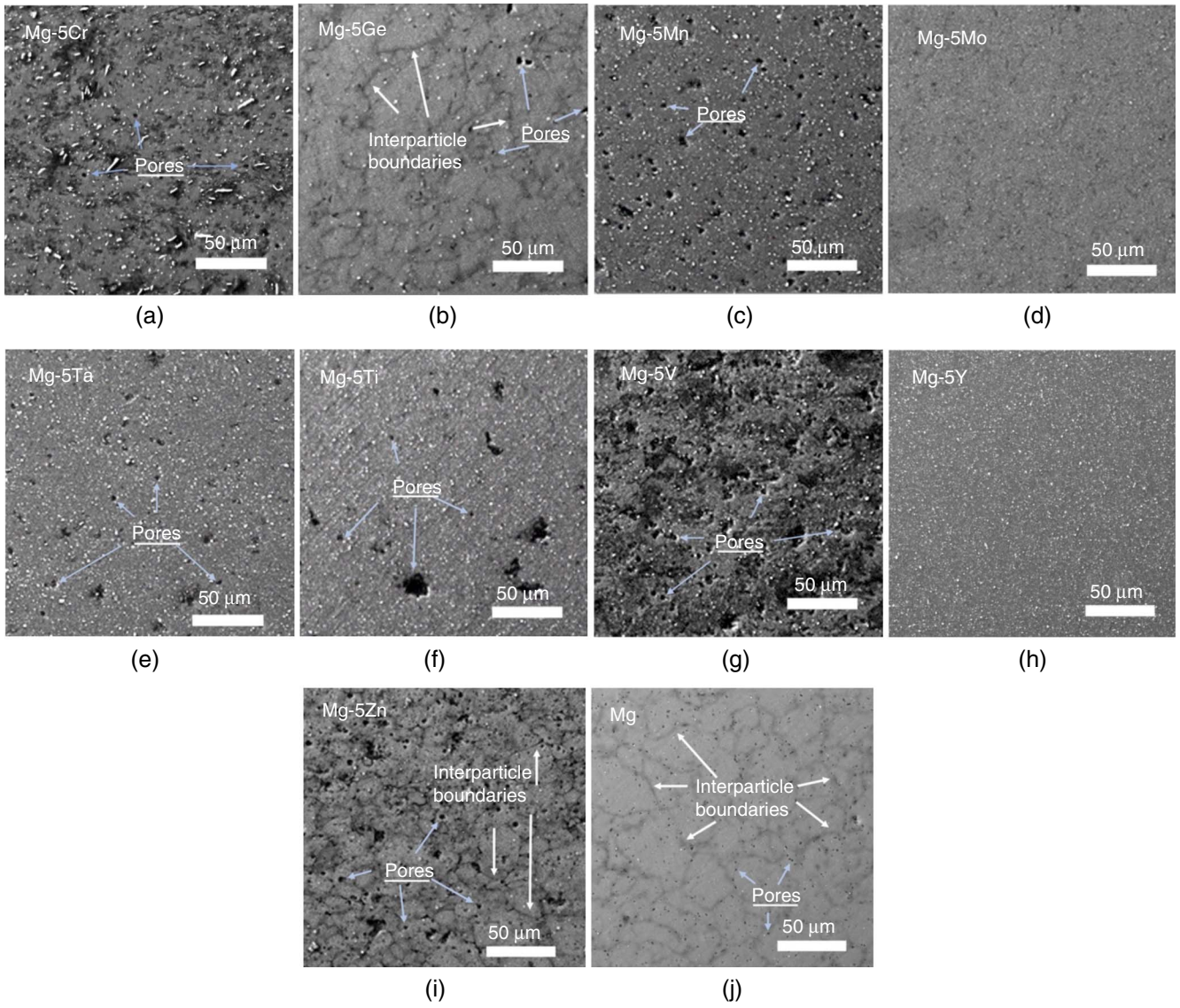

FIGURE 4. *BSE images of Mg-5M alloys in (a) through (i) for cold compacted samples having the addition of Cr, Ge, Mn, Mo, Ta, Ti, V, Y, and Zn, respectively, along with cold-compacted Mg without any addition in (j).*

response of alloys from this work, which will be discussed here. The extent to which the kinetics changed for individual alloying elements has significant scope for unraveling the scientific understanding of elemental influence to Mg. However, at this instant, alloying elements can be grouped based on their general tendency to influence the cathodic reaction kinetics of Mg.

4.2 | Unchanged Cathodic Kinetics

The SPS Mg-5Y alloy showed cathodic kinetics very similar to pure Mg in the milled state; however, the anodic kinetics showed lower anodic current densities on increasing the anodic potential (Figure 8). Previous work showed that the addition of Y as an alloying element by casting increased the cathodic kinetics resulting in overall higher i_{corr},[12] whereas the ball-milled Mg-5Y following SPS showed a reduction in the i_{corr} (Table 1). The unchanged cathodic kinetics can be ascribed to the uniform distribution of Mg_aY_b ($Mg_2Y/Mg_{24}Y_5$), intermetallic as well as elemental Y (Figure 5[i]), in the microstructure.

4.3 | Lower Cathodic Kinetics

The addition of Ge and Zn were the only elements that showed a decrease in the cathodic kinetics, although to different extents (Figure 8). The two elements can be discussed individually. First, the effect of Ge has been explained as cathodic poisoning[11,27] and is suggested to be because of Ge influencing the rate of water dissociation[85] and hydrogen recombination.[11,27,85] These benefits from cathodic poisoning affected the cathodic reaction rate. However, the anodic kinetics are much higher for ball-milled Mg-5Ge alloy. Such behavior is different as the anodic kinetics was suggested to decrease with Ge addition in a recent review.[1] Another study indicates an increase in the anodic current density and interestingly showed an apparent passive window in the range of 0.3 wt% to 1.5 wt% Ge addition but not at 2 wt%.[84] In that work, Ge up to 2 wt% was present as Mg_2Ge intermetallic in rod form between the grain boundaries[84] (Table 1). In this work, a more homogenized microstructure was obtained (Figure 5[a]) and was expected to have decreased anodic kinetics. Instead, high anodic kinetics

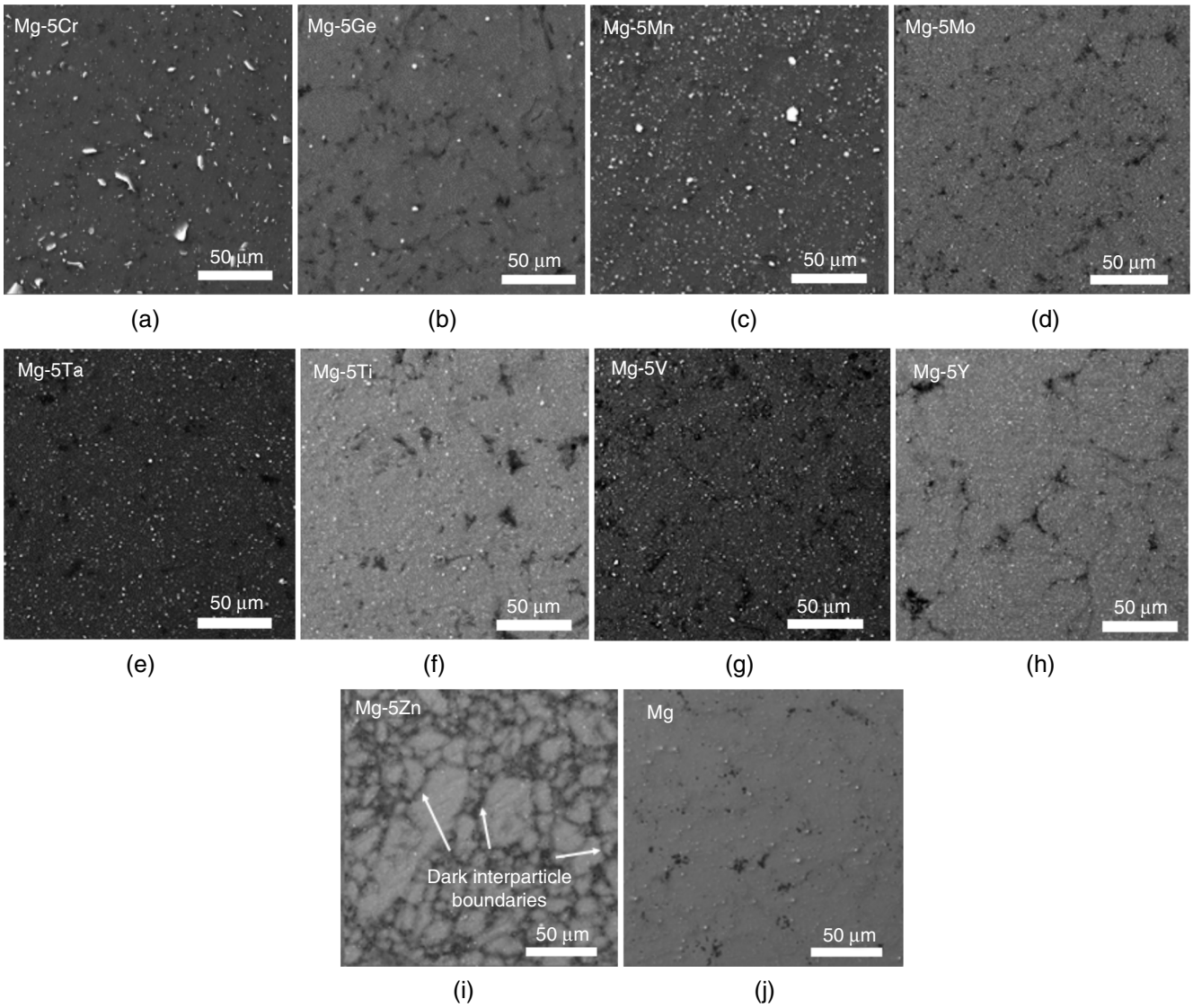

FIGURE 5. *BSE images of Mg-5M alloys in (a) through (i) after SPS (300°C/200 MPa/5 min) with the addition of Cr, Ge, Mn, Mo, Ta, Ti, V, Y, and Zn, respectively, along with SPS Mg without any addition in (j).*

was observed. The absence could be due to a large volume fraction of the Mg_2Ge intermetallic formation for 5 wt% addition of Ge, which is cathodic to the Mg matrix. Thus, at anodic potentials, the current densities are much higher than milled Mg in SPS condition (Figure 8) because of the galvanic effect with nobler Ge and Mg_2Ge intermetallic.[11]

Second, the reduction in the cathodic kinetics in the case of Mg-5Zn is interesting as it has been reported that Zn addition increases the cathodic kinetics for Mg[6,87] (Table 1). A possible factor in the system is the size of the intermetallics. Intermetallic peaks were observed after the SPS of the alloy (Figure 2[b]). However, they were submicrometer-sized particles, as shown in the SEM (Figure 5[i]). Also, 1 wt% Zn addition did not show much difference in the cathodic kinetics but showed ennoblement of E_{corr}.[96] Previous work on ZE41 alloys reported improvement in the corrosion behavior due to grain refinement with a concomitant homogeneous distribution of second phase particles.[57,86] These two features enhanced in the present case due to HEBM. The grain size for Mg-5Zn after SPS is 200 nm (Figure 3). Decreased anodic kinetics of the Mg-5Zn alloy is expected, as has been shown before,[87-88] although for low concentrations of up to 2 wt% and with the weakly polarizing system showing less ennoblement. The electrochemical homogenization has reduced the galvanic effect in anodic kinetics. The ennoblement here (Figure 8) is excellent and could be partly ascribed to significant solid solubility, as indicated from the largest peak shift to higher 2θ values among all alloys presented here (Figure 2[d]).

4.4 | Higher Cathodic Kinetics

4.4.1 | Mn, Cr, and Ta

All three elements, Mn, Cr, and Ta, showed ennoblement of the E_{corr} about 55 mV to 65 mV above Mg along with very similar cathodic and anodic kinetics compared to Mg as shown in Figure 8. Out of these three elements, only Mn has a solubility of 2 wt% in Mg, whereas Cr and Ta have negligible solid solubility. For the ennoblement in all three cases, it could be reasoned that these elements have electrode potential nobler than Mg, and due to uniform distribution through HEBM. The

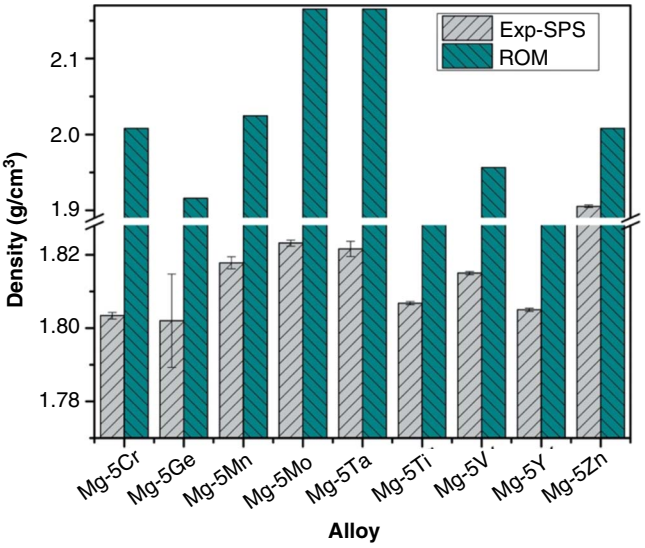

FIGURE 6. *Comparison of experimental and rule of mixture (ROM) densities for SPS samples.*

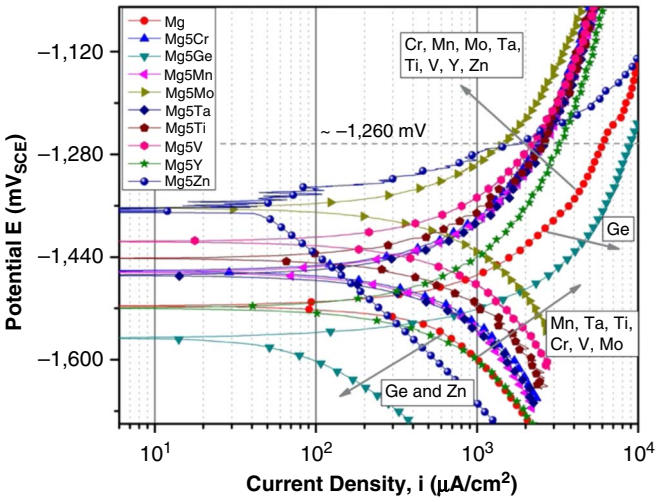

FIGURE 8. *Potentiodynamic polarization data for Mg-5M alloys tested in 0.1 M NaCl solution after spark plasma sintering at 200 MPa/300°C/5 min.*

microstructure was homogenized electrochemically by decreasing the galvanic effect for small particles.

Although Ta (E_0 = –0.2 V_{SHE}) has standard electrode potential close to Mo (E_0 = –0.6 V_{SHE}), compared to others, it did not ennoble the E_{corr} of Mg as much as Mo or Zn addition but was close to the E_{corr} of Mg-5Mn and Mg-5Cr with similar cathodic and anodic kinetics (Figure 8). This difference in ennoblement could be attributed to the difference in the influence on cathodic kinetics of Mg and not due to a lower corrosion rate.[2]

The contrast of the present results with previous studies can be mentioned individually (Table 1). A previous study reports that for the alloys produced through casting, Mn showed decreased cathodic kinetics up to 2 wt% along with an increase in the anodic kinetics.[25] In another study with vapor-deposited Mg-Mn alloy, the corrosion rates were less than Mg for up to 14 wt% addition;[89] however, there were no comments about the reaction kinetics individually. Here, the ball-milled Mg-5Mn alloy following SPS showed higher cathodic kinetics but with decreased anodic kinetics and overall lesser i_{corr} than Mg (Figures 8 and 9). With regard to the Cr addition, magnetically sputtered Mg-xCr alloys were studied in 0.1 M $(NH_4)_3BO_3$+NH_4OH (pH 9.9) using voltammetric curves with a sweep rate of 5 mV/s, suggesting good corrosion resistance when alloying addition reaches one third in composition.[90] If Cr were present in a solid solution, the galvanic effect would be minimized significantly.[89] However, here in 0.1 M NaCl, Mg-5Cr alloy showed lower i_{corr} than Mg in SPS condition (Figure 8). Moreover, Ta sputter deposited on Mg showed improvement in the degradation of Mg resistance in simulated body fluid.[91-92] Here, the ball-milled Mg-5Ta alloy after SPS also showed decreased anodic kinetics and overall lower i_{corr} than SPS Mg (Figures 8 and 9). Overall, in the three cases, a decrease in the i_{corr} was observed because of a significant contribution from decreased anodic kinetics. These results support the controlled dissolution of Mg by the elements, which may be acting as either dissolution moderators (Ta) or passivity promotors (Cr, Mn).[97-98]

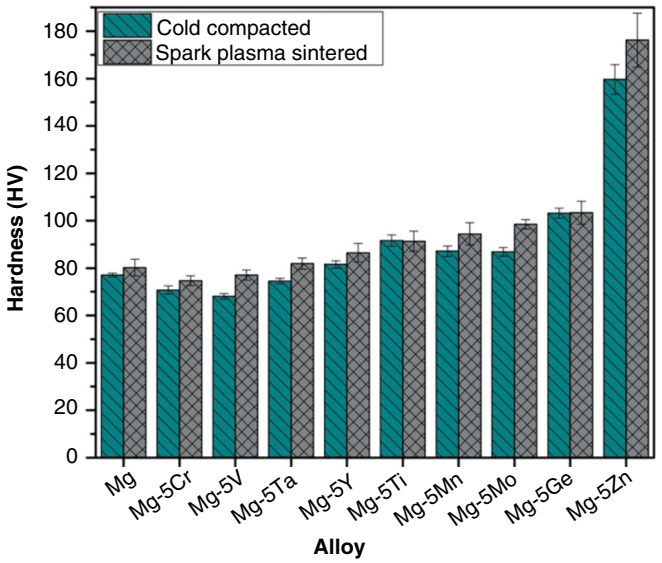

FIGURE 7. *Vickers hardness for cold compacted (CC) and spark plasma sintered (SPS) Mg-5M (M- Cr, Ge, Mn, Mo, Ta, Ti, V, Y, and Zn) alloys.*

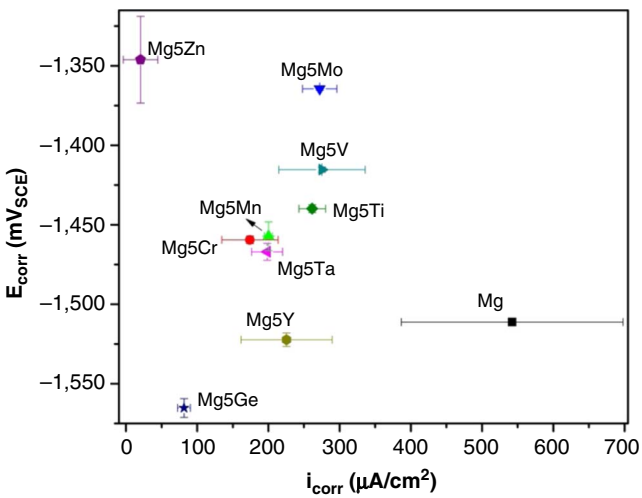

FIGURE 9. *Corrosion current density (i_{corr}) vs. corrosion potential (E_{corr}) plot for Mg-5M alloys after spark plasma sintering (300°C/200 MPa/5 min).*

Table 1. *Key Comparison Between the Work Present in Literature and the Current Work for the Influence of Alloying Additions in Mg on Corrosion Kinetics*

Alloying Element	Examples from Literature	Current Work (5 wt% additions)	Suggested Reasoning
Y	Addition by casting—overall high i_{corr}.[12]	Unchanged potential and cathodic kinetics but overall lower i_{corr}.	Uniform distribution and minor alloying.
Ge	Addition above 2 wt% is deleterious.[84]	Higher anodic kinetics but drastically decreased corrosion kinetics, overall lower i_{corr}.	Uniform distribution of Ge and intermetallic, reduced water dissociation,[85] and hydrogen recombination.[11,27,85]
Zn	Addition increases the cathodic kinetics, ZE41 showed minor ennoblement,[86] and homogenous phase distribution.[77,86] Decreased anodic kinetics.[87-88]	Excellent ennoblement as well as homogeneity, and significantly decreased anodic kinetics.	High solid solubility and homogenous microstructure.
Mn	Negligible solubility at room temperature, maximum solubility 2 wt%, require 14% to have corrosion rate lower than Mg.[89]	Minor alloying, uniform distribution in the matrix, and showed decreased i_{corr}.	Uniform fine distribution in the microstructure, dissolution moderator.
Cr	Negligible solubility at room temp, magnetically sputtered with Cr >33 wt% showed good corrosion resistance.[90]	Minor alloying, uniform distribution of coarse particles but lower i_{corr} than Mg.	Uniform distribution but bigger unalloyed particles.
Ta	No solid solubility; sputtered Ta showed decreased degradation in SBF.[91-92]	Minor alloying, uniform distribution, decreased anodic kinetics with overall lower i_{corr} than Mg.	Uniform fine distribution in the microstructure, dissolution moderator.
Ti	Added to AZ series alloys,[2] increase anodic and decreased cathodic activity with overall minor effect.[93]	Minor alloying, uniform distribution. Ennobled E_{corr} with decreased i_{corr}, increased cathodic kinetics, and decreased anodic kinetics.	Uniform fine distribution in the microstructure, dissolution moderator.
V	Negligible solid solubility, alloy surface prepared by PVD but reaction kinetics not considered.[94]	Minor alloying, peak shift suggest solubility. Ennobled E_{corr} and lower i_{corr} with higher cathodic kinetics.	Uniform fine distribution in the microstructure, dissolution moderator.
Mo	Negligible solid solubility, addition as composite enhanced cathodic kinetics, and minor effect on anodic kinetics.[95] Addition of 0.1 wt% to AZ91E drastically increase i_{corr}.[13]	Minor alloying, uniform distribution, peak shift suggest solubility. Ennobled E_{corr} and lower i_{corr} with higher cathodic kinetics.	Uniform fine distribution in the microstructure, dissolution moderator.

4.4.2 | Ti, V, and Mo

Like Mn, Cr, and Ta, the other three elements Mo, V, and Ti, also showed increased cathodic kinetics and ennobled corrosion potential but with a higher degree. The sequence of the increase can be written as Mg-5Ti < Mg-5V < Mg-5Mo. All three elements have shown a contrasting effect as compared to the previous studies of addition to Mg (Table 1). Previously, Mg and Ti have been mixed using HEBM for making alloys[64] and composites;[65,99] however, such works have not tested their corrosion behavior. Ti has always been added to AZ series alloys, specifically AZ91, for improving the corrosion performance[2] as it helps in modifying the morphology and distribution of the beta phase.[93] For example, in a 0.1 M NaCl, AZ91E with 0.1 wt% Ti addition showed that the anodic activity increased slightly with a concomitant decrease in the cathodic activity; however, the overall reaction rate did not decrease much.[93] In contrast, here, the 5 wt% Ti addition to Mg ennobled the E_{corr} (Figure 9) with a significant decrease in the i_{corr}, increased the cathodic kinetics, and some reduction in anodic kinetics (Figure 8).

V and Mo have scarcely been added as the main alloying elements as they have negligible solid solubility.[1,100] For V, there has been a recent work presenting immersion test data in 3 wt% NaCl for Mg-V alloys developed by physical vapor deposition studying the films formed on the alloy surface; however, reaction kinetics was not considered.[94] Exploration of Mo as an addition to Mg is also scarce. When Mo was added as a composite up to 0.6 wt%, it significantly enhanced the cathodic current kinetics with a minor effect on anodic kinetics in 3.5 wt% NaCl.[95] Also, the low addition of Mo (0.1 wt%) to AZ91E has been indicated to have a drastic increase in the i_{corr} values.[13] However, in the present work, for both the elements, the i_{corr} was lower than the milled Mg (Figure 9). Moreover, the minor alloying for V and Mo addition suggested due to Mg peak shift to lower 2θ values (Figures 1[d] and 2[d]) supports the idea of the contribution of alloying in the ennoblement besides due to an increase in cathodic kinetics. Hence, even though the cathodic kinetics were much higher for V and Mo addition, the corresponding i_{corr} was lower than Mg, which suggests that these elements partially blocked the dissolution of Mg.

These combinations of corrosion behavior as an influence of alloying elements provide support for the conceptual premise that the corrosion rate of Mg is predominantly under kinetic control. From the overall behavior observed, the alloys can be categorized based on the way they are minimizing corrosion: (i) act as cathodic poisoning with tremendously decreased cathodic kinetics—Ge; (ii) significant ennoblement due to alloying with decreased cathodic kinetics, e.g., Zn; (iii) ennoblement due to a combination of some alloying and increase in cathodic kinetics but an attenuated galvanic effect, e.g., Mn, Cr, Ta, Ti, V, Mo; and (iv) negligible ennoblement but decreased anodic kinetics, e.g., Y.

The results could be readily explained considering concepts suggested in literature such as dissolution blockers (or dissolution moderator)[98] and percolation theory.[101-104] Both concepts require surface enrichment of added elements to minimize dissolution. However, the percolation theory necessitates the formation of a connected network,[101-105] whereas the dissolution moderator helps in controlled dissolution without the necessity of a network.[98] Such enrichment was recently investigated for the impurities in Mg.[106-107] For the six elements from the third category and Y from the fourth category, the lowered anodic current kinetics and an indication of solid solubility suggest that they played the role of a dissolution moderator, allowing the controlled dissolution of Mg. The addition of elements with a concentration higher than the solubility limit at room temperature using HEBM and objectively lowered current densities support the percolation theory[101-104,108-109] even though the decrease in the anodic kinetics was not significant. One of the reasons for a limited decrease in the overall i_{corr} values is because of higher cathodic kinetics. It is difficult to comment on the dominance of any one theory based on available information at this point. Overall, the majority of the alloys here showed a uniformly distributed microstructure maintaining electrochemical homogeneity leading to i_{corr} lower than milled Mg after SPS.

4.5 | General Discussion

Many elements have been studied in the last two decades for alloying in Mg.[2] However, there are elements with very negligible (Ge, Mn, and Cr) or no solid solubility (V, Mo, and Ta). Insoluble elements have rarely been studied as an addition in Mg for their effect in corrosion response.[2] Nonequilibrium techniques are useful in creating the solubility. In the present study, even the insoluble elements such as Ta and V come closer to the corrosion kinetics behavior akin to Mn addition into Mg in terms of corrosion current densities. Similarly, Mo addition showed corrosion kinetics close to Ti addition. These new alloys open a significant avenue to explore the possibilities with improved properties for various applications.

Although there are improvements in the corrosion resistance compared to the unalloyed Mg, there is significant scope for process improvement for better alloying and consolidation of the material produced to achieve the best properties. Notwithstanding, the produced alloys are novel as these have not been produced using HEBM. They have been suggested[29-30,110] to enhance the corrosion behavior as well as mechanical properties greatly.

With regard to the mechanical properties, the hardness of Mg improved to varying degrees due to strengthening depending upon the alloying with an individual element and grain refinement. Figure 10 shows the Vicker's hardness with corresponding reciprocal grain size for all of the Mg-5M alloys in cold compacted and SPS conditions. Solid symbols

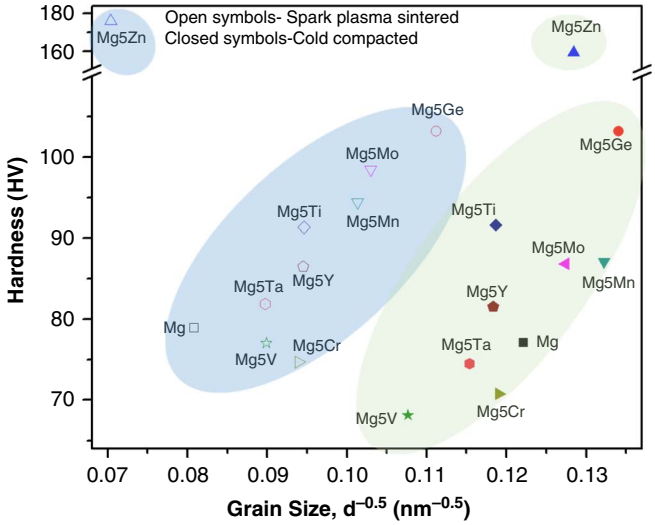

FIGURE 10. *Hardness and grain size (Hall-Petch) for CC (solid symbols) and SPS (open symbols) Mg-5M alloys produced by HEBM.*

denote the data for CC samples, and the open symbols of the same shape indicate the data for SPS samples for respective compositions. Overall, the SPS Mg-5M alloys exhibited higher hardness even though their grain size increased. This information suggests that strengthening is not limited to Hall-Petch strengthening due to grain refinement. There are a couple of other possible factors that might have contributed to strengthening. First, there is an indication of a decrease in the porosity after SPS for most of the alloys, as evident from BSE images, specifically in the case of Mg-Ge, Mg-Mn, Mg-Cr, Mg-V, Mg-Ta, and Mg-Zn. Second, from XRD, it is clear that in SPS samples the second phase peaks evolved more than that of the CC alloys. Thus, there is a possibility of contribution from the precipitates causing Orowan strengthening.[111] Third, there will be a varied contribution of solid solution strengthening. The solid solubility of the alloying elements could not be calculated using XRD data. It should be noted that the Hall-Petch coefficient and therefore strengthening due to grain refinement largely depends on the alloying element in Mg alloys. Hall-Petch coefficients of added elements and corresponding misfit parameters for Mg are summarized in Table S4 of the Supplemental Material. Ti and Zn have lower Hall-Petch coefficients, a higher solid solution contribution could be expected if an increase in the strength is observed. There is an outstanding increase in the hardness for Zn addition with clear evidence of a significant decrease in lattice parameter, there is a possibility of significant solid solution strengthening apart from grain refinement.

Correlating the mechanical strength in terms of hardness with their respective dissolution tendency would give a good idea for the selection of these alloys for specific applications. Figure 11 shows i_{corr} vs Vickers' hardness plot for all of the SPS Mg-5M alloys synthesized by HEBM. In this plot, the favorable alloys would lie toward the bottom right, indicating lower dissolution rates while offering high strength. In this respect, two good candidates are Mg-5Zn with the highest hardness and lowest i_{corr}, followed by Mg-5Ge (Figure 11). On the other hand, Mg-5Cr and Mg-5V are not the best options in terms of strength, although they offer lower dissolution tendencies than milled Mg.

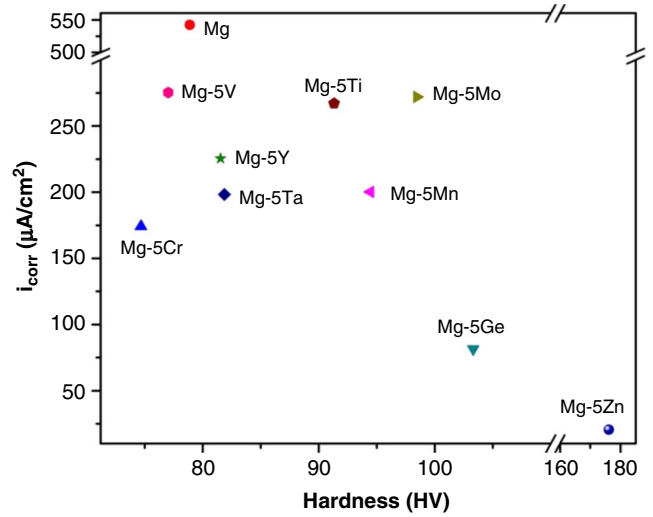

FIGURE 11. *Corrosion current density vs. hardness plot for SPS (300°C/200 MPa/5 min) Mg-5M alloys produced by HEBM.*

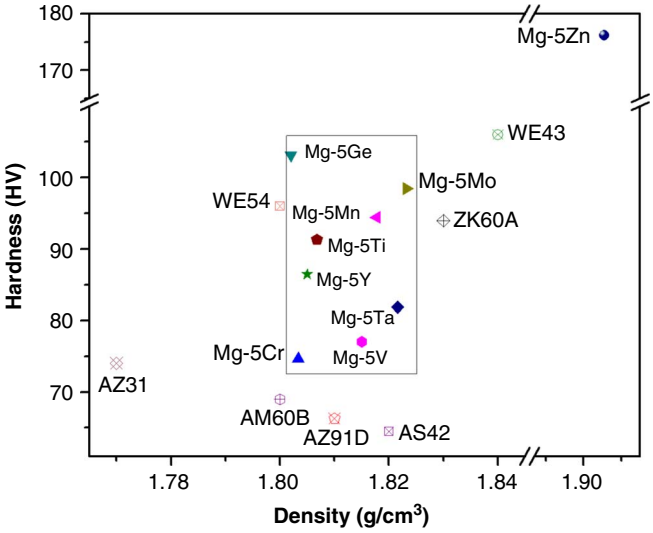

FIGURE 12. *Hardness as a function of density for SPS Mg-5M alloys produced by HEBM in comparison with commercial alloys.*

For comparing the industrial applicability of SPS HEBM-Mg alloys with commercial alloys, the hardness vs. density data are presented in Figure 12. The hardness of most of the binary Mg-5M alloys produced by HEBM is higher than many commercial alloys such as AS42, AZ91D, AM60B, and AZ31 with comparable density (Figure 12). Just a binary Mg-5Ge alloy has hardness close to WE43 alloy, which is the highest among commercial Mg alloys, but with a lower density. The highest Vickers hardness, although with little higher density, was exhibited for Mg-5Zn alloy.

CONCLUSIONS

The study presents various synthesized binary Mg-5M alloys and investigated the microstructure, hardness, density, and corrosion behavior. The results direct several findings from this work.

➢ Nanocrystalline (grain size < 100 nm) Mg-5M (M- Ge, Mn, Ti, Mo, Cr, V, Ta, Y, and Zn) alloys have been synthesized using high-energy ball milling.

➢ Homogeneous microstructure and some alloying in terms of the XRD peak shift were observed. Most of the alloys showed a homogenous microstructure with submicrometer-sized second phases such as Mg-5Ge, Mg-5Ti, Mg-5Mo, Mg-5V, Mg-5Ta, and Mg-5Zn.

➢ Spark plasma sintering improved the consolidation of the alloys with less porous microstructure for most of the alloys.

➢ The study observed improvement in the corrosion behavior of all selected alloys, especially in the case of Mg-5Ge and Mg-5Zn for a kinetically controlled system of Mg.

➢ Considering the kinetics of the cathodic reactions the HEBM Mg-5M SPS alloys can be categorized into three categories: (i) unchanged cathodic kinetics, where a negligible shift in cathodic current densities was seen, e.g., Y addition; (ii) high cathodic kinetics involving elements which greatly influence the cathodic current densities such as Ti, V, and Mo, as well as those with lesser influence in increasing the cathodic kinetics such as Cr, Mn, and Ta; and (iii) low cathodic kinetics, including both cathodic poisoning effect of Ge and tremendous effect of the solid solution by Zn addition.

➢ Considering the anodic kinetics, besides Ge and Zn, all other alloying elements decreased the anodic kinetics of Mg as a potential indication for blocking or moderating the dissolution of Mg.

➢ Many of the binary alloys showed hardness comparable to commercially available Mg alloys. The hardness of all of the Mg-5M alloys was improved even after SPS, which in general led to an increase in the grain size, indicating the presence of strengthening mechanisms other than the grain refinement.

➢ The produced binary alloys herein are comparable in density and corrosion resistance to commercial alloys but with improved hardness, especially in the case of Mg-5Zn followed by Mg-5Ge.

ACKNOWLEDGMENTS

RKG acknowledges the financial support from the National Science Foundation (NSF-CMMI 1846887) under the direction of Dr. Alexis Lewis.

References

1. M. Esmaily, J.E. Svensson, S. Fajardo, N. Birbilis, G.S. Frankel, S. Virtanen, R. Arrabal, S. Thomas, L.G. Johansson, *Prog. Mater. Sci.* 89 (2017): p. 92-193.
2. K. Gusieva, C.H.J. Davies, J.R. Scully, N. Birbilis, *Int. Mater. Rev.* 60 (2015): p. 169-194.
3. C.H. Caceres, *Metall. Mater. Trans. A Phys. Metall. Mater. Sci.* 38A (2007): p. 1649-1662.
4. S.N. Khan, R.M. Warkhedkar, A.K. Shyam, *Sadhana - Acad. Proc. Eng. Sci.* 40 (2015): p. 1667-1679.
5. M. Navarro, A. Michiardi, O. Castaño, J.A. Planell, M. Navarro, A. Michiardi, O. Castan, *J. R. Soc. Interface* 5 (2008): p. 1137-1158.
6. N.T. Kirkland, M.P. Staiger, D. Nisbet, C.H.J. Davies, N. Birbilis, *JOM* 63 (2011): p. 28-34.
7. L. Yin, X. Huang, H. Xu, Y. Zhang, J. Lam, J. Cheng, J.A. Rogers, *Adv. Mater.* 26 (2014): p. 3879-3884.
8. V. Edupuganti, R. Solanki, *J. Power Sources* 336 (2016): p. 447-454.
9. J.O. Bockris, A.K.N. Reddy, *Modern Electrochemistry 2B*, 2nd ed. (New York, NY: Kluwer Academic Publishers, 2004).
10. T. Cain, L.G. Bland, N. Birbilis, J.R. Scully, *Corrosion* 70 (2014): p. 1043-1051.
11. R.L. Liu, M.F. Hurley, A. Kvryan, G. Williams, J.R. Scully, N. Birbilis, *Sci. Rep.* 6 (2016): p. 1-12.
12. A.D. Sudholz, K. Gusieva, X.B. Chen, B.C. Muddle, M.A. Gibson, N. Birbilis, *Corros. Sci.* 53 (2011): p. 2277-2282.

13. A.D. Südholz, N. Birbilis, C.J. Bettles, M.A. Gibson, *J. Alloys Compd.* 471 (2009): p. 109-115.
14. A.D. Südholz, N.T. Kirkland, R.G. Buchheit, N. Birbilis, *Electrochem. Solid-State Lett.* 14 (2011): p. 2010-2012.
15. G.S. Frankel, A. Samaniego, N. Birbilis, *Corros. Sci.* 70 (2013): p. 104-111.
16. N. Birbilis, A.D. King, S. Thomas, G.S. Frankel, J.R. Scully, *Electrochim. Acta* 132 (2014): p. 277-283.
17. M. Taheri, J.R. Kish, N. Birbilis, M. Danaie, E.A. McNally, J.R. McDermid, *Electrochim. Acta* 116 (2014): p. 396-403.
18. G. Song, A. Atrens, X. Wu, B. Zhang, *Corros. Sci. 40* (1998): p. 1769-1791.
19. L. Geng, H.W. Zhang, H.Z. Li, L.N. Guan, L.J. Huang, *Trans. Nonferrous Met. Soc. China* 20, 10 (2010): p. 1851-1855.
20. J. Bai, Y. Sun, F. Xue, J. Qiang, *Mater. Sci. Eng. A* 552 (2012): p. 472-480.
21. G. Gonzalez-doncel, J. Wolfenstine, P. Metenier, O.A. Ruano, O.D. Sherby, *J. Mater. Sci.* 25 (1990): p. 4535-4540.
22. A.K. Chaubey, S. Scudino, M. Samadi Khoshkhoo, K.G. Prashanth, N.K. Mukhopadhyay, B.K. Mishra, J. Eckert, *J. Alloys Compd.* 610 (2014): p. 456-461.
23. D.H. Choi, B.W. Ahn, D.J. Quesnel, S.B. Jung, *Intermetallics* 35 (2013): p. 120-127.
24. C. Blawert, D. Fechner, D. Höche, V. Heitmann, W. Dietzel, K.U. Kainer, P. Živanović, C. Scharf, A. Ditze, J. Gröbner, R. Schmid-Fetzer, *Corros. Sci.* 52 (2010): p. 2452-2468.
25. D.S. Gandel, M.A. Easton, M.A. Gibson, N. Birbilis, *Corrosion* 69 (2013): p. 744-751.
26. I.P. Polmear, *Light Alloys - From Traditional Alloys to Nanocrystals*, 4th ed. (Oxford, England: Elsevier B.H., 2006).
27. R.L. Liu, J.R. Scully, G. Williams, N. Birbilis, *Electrochim. Acta* 260 (2018): p. 184-195.
28. R.K. Gupta, D. Fabijanic, R. Zhang, N. Birbilis, *Corros. Sci.* 98 (2015): p. 643-650.
29. R.K. Gupta, D. Fabijanic, T. Dorin, Y. Qiu, J.T. Wang, N. Birbilis, *Mater. Des.* 84 (2015): p. 270-276.
30. J. Esquivel, H. Murdoch, K. Darling, R. Gupta, *Mater. Res. Lett.* 6 (2018): p. 79-83.
31. R.K. Gupta, R. Zhang, C.H.J. Davies, N. Birbilis, *Corrosion* 70 (2014): p. 402-413.
32. N.L. Sukiman, R.K. Gupta, R.G. Buchheit, N. Birbilis, *Corros. Eng. Sci. Technol.* 49 (2014): p. 254-262.
33. R.K. Gupta, Y. Wang, R. Zhang, N.L. Sukiman, C.H.J. Davies, N. Birbilis, *Corrosion* 69 (2013): p. 4-8.
34. R.K. Gupta, C. Li, J. Xia, X. Zhou, G. Sha, B. Gun, S.P. Ringer, N. Birbilis, *Adv. Eng. Mater.* 17 (2015): p. 1670-1674.
35. D.Y. Liu, J.F. Li, Y.L. Ma, R.K. Gupta, N. Birbilis, R. Zhang, *Corros. Sci.* 145 (2018): p. 220-231.
36. N. Birbilis, R.G. Buchheit, *J. Electrochem. Soc.* 152 (2005): p. B140.
37. G.M. Scamans, N. Birbilis, R.G. Buchheit, "Corrosion of Aluminum and its Alloys," in *Shreir's Corrosion,* ed. T. Richardson (Amsterdam, Netherlands: Elsevier, 2010), p. 1974-2010.
38. P.L. Miller, B.A. Shaw, R.G. Wendt, W.C. Moshier, *Corrosion* 51 (1995): p. 922-931.
39. H. Altun, S. Sen, *Surf. Coat. Technol.* 197 (2005): p. 193-200.
40. W.C. Moshier, *J. Electrochem. Soc.* 133 (1986): p. 1063.
41. W.C. Moshier, *J. Electrochem. Soc.* 134 (1987): p. 2677.
42. G.D. Davis, B.A. Shaw, B.J. Rees, C.A. Pecile, *Surf. Interface Anal.* 23 (1995): p. 609-617.
43. Q. Yan, H. Yoshioka, H. Habazaki, A. Kawashima, K. Asami, K. Hashimoto, *Corros. Sci.* 31 (1990): p. 401-406.
44. M.G. Ward, "Filling of Vias and Contacts Employing an Aluminum-Germanium Alloy," U.S. Patent 5358616, 1994.
45. X. Wang, X. Zeng, G. Wu, S. Yao, *Mater. Lett.* 61 (2007): p. 968-970.
46. C. Liu, Y. Xin, X. Tian, J. Zhao, P.K. Chu, *J. Vac. Sci. Technol. A* 25 (2007): p. 334-339.
47. P.M. Natishan, E. McCafferty, G.K. Hubler, *Corros. Sci.* 32 (1991): p. 721-731.
48. J.M. Williams, A. Gonzales, J. Quintana, I.S. Lee, R.A. Buchanan, F.C. Burns, R.J. Culbertson, M. Levy, J.R. Treglio, *Nucl. Instrum. Methods Phys. Res. B* 59-60 (1991): p. 845-850.
49. G. Wu, R. Xu, K. Feng, S. Wu, Z. Wu, G. Sun, G. Zheng, G. Li, P.K. Chu, *Appl. Surf. Sci.* 258 (2012): p. 7651-7657.
50. Y.Z. Wan, G.Y. Xiong, H.L. Luo, F. He, Y. Huang, Y.L. Wang, *Appl. Surf. Sci.* 254 (2008): p. 5514-5516.
51. X. Wang, X. Zeng, G. Wu, S. Yao, Y. Lai, *J. Alloys Compd.* 437 (2007): p. 87-92.
52. M. Jamesh, G. Wu, Y. Zhao, P.K. Chu, *Corros. Sci.* 69 (2013): p. 158-163.
53. G.-L. Song, K.A. Unocic, H. Meyer, E. Cakmak, M.P. Brady, P.E. Gannon, P. Himmer, Q. Andrews, *Corros. Sci.* 104 (2016): p. 36-46.
54. K. Schlüter, Z. Shi, C. Zamponi, F. Cao, E. Quandt, A. Atrens, *Corros. Sci.* 78 (2014): p. 43-54.
55. M. Zeller, J. Kargol, *Appl. Surf. Sci.* 18 (1984): p. 63-85.
56. C. Op't Hoog, N. Birbilis, Y. Estrin, *Adv. Eng. Mater.* 10 (2008): p. 579-582.
57. J. Jiang, A. Bin Ma, N. Saito, Z. Shen, D. Song, F. Lu, Y. Nishida, D. Yang, P. Lin, *J. Rare Earths* 27 (2009): p. 848.
58. D. Song, A. Bin Ma, J. Jiang, P. Lin, D. Yang, J. Fan, *Corros. Sci.* 52 (2010): p. 481-490.
59. R.K. Gupta, N. Birbilis, *Corros. Sci.* 92 (2015): p. 1-15.
60. J. May, M. Dinkel, D. Amberger, H.W. Höppel, M. Göken, *Metall. Mater. Trans. A Phys. Metall. Mater. Sci.* 38A (2007): p. 1941-1945.
61. M.K. Chung, Y.S. Choi, J.G. Kim, Y.M. Kim, J.C. Lee, *Mater. Sci. Eng. A* 366, 2 (2004): p. 282-291.
62. J. Jiang, A. Ma, D. Song, D. Yang, J. Shi, K. Wang, L. Zhang, J. Chen, *J. Mater. Sci.* 47 (2012): p. 7744-7750.
63. J.H. Jiang, A.B. Ma, F.M. Lu, N. Saito, A. Watazu, D. Song, P. Zhang, Y. Nishida, *Mater. Corros.* 62 (2011): p. 848-852.
64. G. Liang, R. Schulz, *J. Mater. Sci.* 38 (2003): p. 1179-1184.
65. Z. Haiping, H. Lianxi, S. Hongfei, C. Xianjue, *Mater. Charact.* 106 (2015): p. 44-51.
66. G.X. Liang, R. Schulz, *J. Metastable Nanocrystalline Mater.* 12 (2002): p. 93-110.
67. E.M. Salleh, S. Ramakrishan, Z. Hussain, *Adv. Mater. Res.* 1087 (2015): p. 479-483.
68. J. Bystrzycki, T. Czujko, R.A. Varin, *J. Alloys Compd.* 404-406 (2005): p. 507-510.
69. C.R. Clark, C. Wright, C. Suryanarayana, E.G. Baburaj, F.H. Froes, *Mater. Lett.* 33 (1997): p. 71-75.
70. A.L. Patterson, *Phys. Rev.* 56 (1939): p. 978-982.
71. K. Nakajima, A. Fujiyoshi, Z. Ming, M. Suzuki, K. Kimura, *J. Appl. Phys.* 102 (2007): p. 2005-2008.
72. Z.Z. Fang, J.D. Paramore, P. Sun, K.S.R. Chandran, Y. Zhang, Y. Xia, F. Cao, M. Koopman, M. Free, *Int. Mater. Rev.* 63 (2018): p. 407-459.
73. K. Takamura, Y. Abe, K. Sasaki, *Vacuum* 74 (2004): p. 397-401.
74. C.J. Cabral, L.A. Clevenger, R.G. Schad, *Mater. Res. Soc. Symp. Proc.* 308 (1993): p. 57-61.
75. S. Couet, J. Swerts, S. Mertens, T. Lin, Y. Tomczak, E. Liu, B. Douhard, S. Van Elshocht, A. Furnemont, G.S. Kar, *IEEE Magn. Lett.* 7 (2016): p. 5-8.
76. M. Efe, H.J. Kim, S. Chandrashekhar, K.P. Trumble, *Mater. Sci. Eng. A* (2012): p. 1-10.
77. C.E. Johnson, D.C. Fee, *Nucl. Technol.* 40 (1978): p. 89-97.
78. C.A. Neugebauer, R.A. Ekvall, *J. Appl. Phys.* 35 (1964): p. 547-553.
79. M. Wu, J. Moulin, P. Coste, S. Perrot, J.L. Perrosier, *Thin Solid Films* 616 (2016): p. 1-8.
80. D.C. Ghosh, R. Biswas, *Int. J. Mol. Sci.* 3 (2002): p. 87-113.
81. A. Becerra, M. Pekguleryuz, *J. Mater. Res.* 23 (2008): p. 3379-3386.
82. I.M. Young, *J. Mater. Sci.* 14 (1979): p. 1579-1585.
83. S. Cai, T. Lei, N. Li, F. Feng, *Mater. Sci. Eng. C* 32 (2012): p. 2570-2577.
84. B. Kim, K. Park, H. Kimura, Y. Park, I. Park, *Mater. Trans.* 53 (2012): p. 240-243.
85. K.R. Limmer, K.S. Williams, J.P. Labukas, J.W. Andzelm, *Corrosion* 73 (2017): p. 506-517.
86. D. Orlov, K.D. Ralston, N. Birbilis, Y. Estrin, *Acta Mater.* 59 (2011): p. 6176-6186.
87. X. Xia, J.F. Nie, C.H.J. Davies, W.N. Tang, S.W. Xu, N. Birbilis, *Corrosion* 71 (2015): p. 1370-1386.
88. Y. Song, E.H. Han, D. Shan, C.D. Yim, B.S. You, *Corros. Sci.* 65 (2012): p. 322-330.
89. K.R. Baldwin, D.J. Bray, G.D. Howard, R.W. Gardiner, *Mater. Sci. Technol.* 12 (1996): p. 937-943.

90. M. Samulevičien, P. Miečinskas, K. Leinartas, A. Grigucevičien, P. Kalinauskas, V. Jasulaitien, R. Jušknas, E. Juzeliūnas, *Mater. Chem. Phys.* 126 (2011): p. 898-903.
91. W. Jin, G. Wang, Z. Lin, H. Feng, W. Li, X. Peng, A.M. Qasim, P.K. Chu, *Corros. Sci.* 114 (2017): p. 45-56.
92. B. Singh, G. Singh, B.S. Sidhu, *J. Compos. Mater.* 53 (2019): p. 2661-2673.
93. X. Ai, G. Quan, *Open Mater. Sci. J.* 6 (2012): p. 6-13.
94. S. Diplas, P. Tsakiropoulos, R.M.D. Brydson, J.F. Watts, *Mater. Sci. Technol.* 14 (1998): p. 699-711.
95. S.B. Abhijit, R. Balasubramaniam, M. Gupta, *Corros. Sci.* 50 (2008): p. 2423-2428.
96. R.L. Liu, Z.R. Zeng, J.R. Scully, G. Williams, N. Birbilis, *Corros. Sci.* 140 (2018): p. 18-29.
97. C.D. Taylor, P. Lu, J. Saal, G.S. Frankel, J.R. Scully, *Npj Mater. Degrad.* 2 (2018): article 6.
98. P. Marcus, *Corros. Sci.* 36 (1994): p. 2155-2158.
99. M. Rashad, F. Pan, M. Asif, J. She, A. Ullah, *J. Magnes. Alloy.* 3 (2015): p. 1-9.
100. T.B. Massalski, J.L. Murray, L.H. Bennett, H. Baker, *Binary Alloy Phase Diagrams*, vol. 2 (Materials Park, OH: ASM International, 1986).
101. K. Sieradzki, R.C. Newman, *J. Electrochem. Soc.* 133 (1986): p. 1979.
102. R.C. Newman, F.T. Meng, K. Sieradzki, *Corros. Sci.* 28 (1988): p. 523-527.
103. D.M. Artymowicz, J. Erlebacher, R.C. Newman, *Philos. Mag.* 89 (2009): p. 1663-1693.
104. D.E. Williams, R.C. Newman, Q. Song, R.G. Kelly, *Nature* 350 (1991): p. 216-219.
105. E. McCafferty, *Corros. Sci.* 50 (2008): p. 3622-3628.
106. N. Birbilis, T. Cain, J.S. Laird, X. Xia, J.R. Scully, A.E. Hughes, *ECS Electrochem. Lett.* 4 (2015): p. C34-C37.
107. P. Gore, T.W. Cain, J. Laird, J.R. Scully, N. Birbilis, V.S. Raja, *Corros. Sci.* 151 (2019): p. 206-218.
108. S. Qian, R.C. Newman, R.A. Cottis, K. Sieradzki, *J. Electrochem. Soc.* 137 (1990): p. 435-439.
109. R.C. Newman, *J. Electrochem. Soc.* 133 (1986): p. 1979-1980.
110. R.K. Gupta, B.S. Murty, N. Birbilis, *An Overview of High-Energy Ball Milled Nanocrystalline Aluminum Alloys* (Cham, Switzerland: Springer, 2017).
111. K.A. Darling, A.J. Roberts, L. Armstrong, D. Kapoor, M.A. Tschopp, L.J. Kecskes, S.N. Mathaudhu, *Mater. Sci. Eng. A* 589 (2014): p. 57-65.